JOURNAL OF AIRCRAFT
Vol. 32, No. 1, January–February 1995

# CFD Optimization of a Theoretical Minimum-Drag Body

Samson Cheung,* Philip Aaronson,† and Thomas Edwards‡
*NASA Ames Research Center, Moffett Field, California 94035*

**This article describes a methodology behind coupling a fast, parabolized Navier-Stokes flow solver to a nonlinear constrained optimizer. The design parameters, constraints, grid refinement, behavior of the optimizer, and flow physics related to the CFD calculations are discussed. Pressure drag reduction in the supersonic regime of a theoretical minimum-drag body of revolution is performed. Careful selection of design variables allows the optimization process to improve the aerodynamic performance. A calculation including nonlinear and viscous effects produces a different minimum drag geometry than linear theory and results in a drag reduction of approximately 4%. Effect of grid density on the optimization process is also studied. In order to obtain accurate optimization results, CFD calculations must model physical phenomena that contribute to the optimization parameters.**

## Introduction

FOR the past two decades, many different approaches have been developed to design aircraft with better aerodynamic performance.[1] Some of these techniques fall into the general category of inverse design methods.[2,3] The quality of the optimized shape obtained from this method depends on the distribution, usually pressure, it is required to match. Therefore, this approach depends on the knowledge of the designer to establish a desirable optimum. In addition, the inverse method does not lend itself to the imposition of constraints. A different approach is called shape perturbation method.[4–6] In this method, an analysis code is coupled with a numerical optimizer to find a shape that optimizes the objective function. This method may be computationally expensive because of the gradient evaluations, which require CFD calculations. Recently, intelligent methods such as the one-shot method[7,8] and the control-based method[9] have merged that yield rapid convergence to the design shape. Unfortunately, these two methods make use of the governing equations of the CFD code; therefore, recoding is needed for different objective functions, boundary conditions, and flow solvers. The methods cannot immediately take advantage of existing validated analysis codes that have already been developed.

A shape perturbation method is chosen for optimization in the present study. An efficient CFD flow solver is coupled with an optimizer for use as a tool in aerodynamic design. Careful selection of design variables allows fast convergence in the optimization process and yields improvements in aerodynamic performance. The present method takes advantage of a Fourier sine series that defines the original body. The Fourier coefficients are convenient, physically relevant design variables for the problem studied here.

As a test case, the Haack-Adams[10–12] (H-A) theoretical minimum-drag body of revolution is chosen. The H-A body is selected in this study because it is a classic aerodynamics problem for which validating experimental data[13] are available. Because of its simple geometry, running large numbers of cases in a grid refinement study is still relatively inexpensive. Since the geometry ends in a finite base, it is particularly well-suited for space-marching codes. By including viscous and other nonlinear effects, it is hoped that a new optimum may be determined.

In the following sections, the H-A body is first derived and then the CFD flow solver is validated on the geometry over a range of Mach numbers and grid densities. Then, the optimization procedure is described, including optimizer behavior, design variable studies, and the constraints used. Finally, grid refinement study of the optimizer/flow solver is completed on the H-A body and the results are presented.

## Haack-Adams Body

The H-A body is a classic aerodynamic shape derived from supersonic slender-body theory. This body was chosen as an optimization test case for its data base of experimental data[13] that can be used to verify the CFD code. The simplicity of the geometry makes grid generation relatively easy and robust. The finite base of the H-A body facilitates correlation with experimental models that have an attached sting, and simplifies modeling with space-marching codes. Slender-body theory, which was used in deriving the H-A body shapes, is a special case of small perturbation potential-flow theory with the additional restriction that the product $r\sqrt{M_\infty^2 - 1}$ is much smaller than $x$, where $r$ is the radius of the body at some streamwise distance $x$ along the axis of the body, and $M_\infty$ is the freestream Mach number. The theory described in this section can be found in most classical aerodynamic textbooks,[14,15] but is reviewed here for convenience. Consider supersonic flow of velocity $U$ and density $\rho_\infty$ over a body of revolution of length $L$. The velocity potential due to a linear source distribution of strength $Uf(x)$ is

$$\Phi(x) = -\frac{1}{2\pi}\int_0^{(x-\beta r)} \frac{f(\xi)}{(x-\xi)^2 - \beta^2 r^2}\,d\xi$$

where $\beta = \sqrt{M_\infty^2 - 1}$, and $x = L(1 + \cos\theta)/2$.

Expressing $f$ as a Fourier sine series

$$f(\theta) = L\sum_{n=1}^{\infty} \alpha_n \sin(n\theta)$$

The derivative of the cross-sectional area $A'$ can be approximated by $f$. Integrating $f$ produces

$$A(\theta) = \frac{L^2}{4}\left\{\alpha_1\left(\pi - \theta + \frac{1}{2}\sin 2\theta\right) + \alpha_2\frac{4}{3}\sin^3\theta + \sum_{n=3}^{\infty}\alpha_n\left[\frac{\sin(n-1)\theta}{n-1} - \frac{\sin(n+1)\theta}{n+1}\right]\right\} \quad (1)$$

Presented as Paper 93-3421 at the AIAA Applied Aerodynamics Conference, Monterey, CA, Aug. 9–11, 1993; received Feb. 1, 1994; revision received May 28, 1994; accepted for publication May 28, 1994. 

*Research Scientist, MCAT Institute. Member AIAA.
†Junior Research Scientist, MCAT Institute.
‡Assistant Chief, Computational Aerosciences Branch. Senior Member AIAA.

Slender-body theory gives the formula of wave drag

$$D_w = \frac{\pi\rho_\infty U^2 L^2}{8} \sum_{n=1}^{\infty} n\alpha_n^2 \tag{2}$$

Equations (1) and (2) show that the cross-sectional area and the wave drag are independent of the Mach number. The H-A body is defined by the body shape that minimizes $D_w$, subject to the following conditions:

C1 = the area at the base $A(L) = A_{\text{base}}$ is fixed and non-zero
C2 = the slope of the body is zero at the base, $dA/dx|_{x=L} = 0$
C3 = the fineness ratio $L/2r_{\max}$ is fixed

It is easy to check that Eq. (1) satisfies C2. The remaining two conditions C1 and C3 determine the values of $\alpha_1$ and $\alpha_2$. In order for a body to produce minimum drag, Eq. (2) suggests that $\alpha_n = 0$ for $n \geq 3$. Condition C1 gives

$$\alpha_1 = 4A_{\text{base}}/L^2\pi \tag{3}$$

and C3 gives $x_{\max}$, the location of the maximum thickness, and therefore

$$\alpha_2 = \alpha_1/2 \cos\theta_{\max}, \qquad \cos\theta_{\max} = (2x_{\max}/L) - 1 \tag{4}$$

## Optimization Procedure

The optimizer first generates a baseline objective function from the initial values of the design variables supplied as input. The optimizer then looks for the gradient direction by perturbing each of the design variables. During each perturbation, a surface grid and computational grid are generated. The flow is then solved on the computational grid, and from this the objective function is produced. The optimizer continues to perturb and search until a set of design variables, and thus a new body shape, is obtained with a local minimum objective function. Both linear and nonlinear constraints can be imposed on the design variables.

### Design Variables

Perturbations are performed through the use of design variables that have a direct influence on the objective function. The design variables used here were inspired by the original Fourier sine series used in the derivation of the H-A body. Equation (1) can be rewritten, using Eqs. (3) and (4), as radius distribution $r$

$$\frac{r^2}{r_{\max}^2} = \frac{A_{\text{base}}}{\pi A_{\max}}\left\{\left(\pi - \theta + \frac{1}{2}\sin 2\theta\right) + \gamma_1 \frac{4}{3}\sin^3\theta + \sum_{m=2}^{\infty} \gamma_m \left[\frac{\sin m\theta}{m} - \frac{\sin(m+2)\theta}{m+2}\right]\right\} \tag{5}$$

where $\gamma_m = \alpha_m/\alpha_1$ for $m = 2, 3, \ldots, \infty$; $r_{\max}$ and $A_{\max}$ are maximum radius and area, respectively. Notice that $r_{\max}$ and $A_{\text{base}}/A_{\max}$ are known. According to linear theory, the $\gamma_m$ are set to zero. However, since nonlinear effects are included in the CFD analysis, a finite number of these coefficients ($m = 2, 3, \ldots, N$) were chosen as the design variables. Therefore, the optimized configuration will also be defined by Eq. (5).

### Constraints

It is important to check that this optimal configuration satisfies the three conditions (C1, C2, and C3) of the H-A body. It is clear that Eq. (5) satisfies C1 when evaluated at $\theta = 0$. Consider

$$\frac{dA}{d\theta}\frac{d\theta}{dx} = -\frac{2A_{\text{base}}}{LA_{\max}}\left\{-\frac{2\sin^2\theta}{\sin\theta} + \gamma_1 \frac{4\sin^2\theta\cos\theta}{\sin\theta} + \sum_{m=2}^{N} \gamma_m \left[\frac{\cos m\theta - \cos(m+2)\theta}{\sin\theta}\right]\right\} \tag{6}$$

Equation (6) is zero when evaluated at $\theta = 0$. Note that the terms inside the summation sign are zero by L'Hopital's rule, thus, C2 is satisfied. From Eq. (1) [or (5)], and the fact that $\alpha_n = 0$ ($n > 2$), it is seen that for a fixed fineness ratio (C3), there is a corresponding value of $x_{\max}$. In the optimization process, the $\alpha_n$, $n > 2$, (design variables) were not zero; therefore, the derivative of $A$ at $x_{\max}$ was not zero. In order to prevent excessive skewness in the CFD grid, the following constraint was imposed $-1 \leq dA/dx|_{x=x_{\max}} \leq 1$, that is

$$\left| -2\sin^2\theta_{\max} + 4\gamma_1 \sin^2\theta_{\max}\cos\theta_{\max} + \sum_{m=2}^{N} \gamma_m[\cos m\theta_{\max} - \cos(m+2)\theta_{\max}] \right| \leq 1 \tag{7}$$

An additional requirement is needed to ensure that the radius of the optimal body [Eq. (5)] is always greater than or equal to zero, i.e.,

$$\left(\pi - \theta + \frac{1}{2}\sin 2\theta\right) + \gamma_1 \frac{4}{3}\sin^3\theta + \sum_{m=2}^{\infty} \gamma_m \left[\frac{\sin m\theta}{m} - \frac{\sin(m+2)\theta}{m+2}\right] \geq 0 \tag{8}$$

for all $0 \geq \theta \geq \pi$. Equations (7) and (8) set the relationships among the $\gamma$ and are treated as constraints for the optimization problem. It should be noted that due to the Fourier nature of the shape functions, the volume of the optimal body [Eq. (5)] is the same as that of the original H-A body.

### Flow Solver

The implemented CFD flow solver is the three-dimensional parabolized Navier-Stokes code, UPS3D.[16] This is a space-marching code that calculates steady-state viscous or inviscid solutions to supersonic flows. A conic approximation is made for the initial marching plane. This code is further supported by a hyperbolic grid generation scheme[17] that is sufficiently fast and robust to operate within an automated optimization environment. In this study, both viscous and inviscid supersonic calculations are employed. From these solutions, the drag coefficient $C_D$ is calculated by integrating pressure and skin friction (if applicable) over the surface of the body. The UPS3D code uses a step size of 0.1% of the body length $L$ on a nominal grid of 21 points in the circumferential direction and 50 points in the body-normal direction. The grid points are clustered near the body surface. Figure 1 illustrates a typical grid used by UPS3D, which shows the surface as well as a plane normal to the body.

### Objective Function

Five design variables, namely, $\gamma_2, \gamma_3, \ldots, \gamma_6$ of Eq. (5) are used in the majority of the remainder of this study. At each step, the optimizer alters the $\gamma$ values and a new shape is defined. A new computational grid is then created and UPS3D calculates the flow over this new geometry. The wave drag coefficient $C_{D_w}$ is determined by numerical integration of the pressure coefficient $Cp$ over the body. If skin friction as well as pressure is included in the integration, then total drag is calculated.

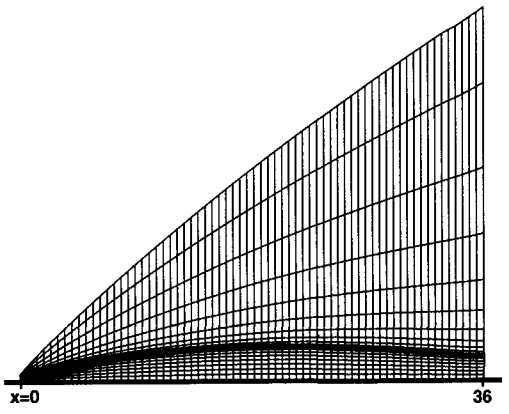


Fig. 1 Schematic marching grid of the H-A body.

### Optimizer

The optimizer, NPSOL,[18] is a collection of Fortran subroutines designed to solve the nonlinear programming problem:

$$\text{minimize } F(\boldsymbol{x})$$

$$\text{subject to } \boldsymbol{l} \leq \begin{bmatrix} \boldsymbol{x} \\ A\boldsymbol{x} \\ c(\boldsymbol{x}) \end{bmatrix} \leq \boldsymbol{u}$$

where $F(\boldsymbol{x})$ is the objective function, $\boldsymbol{x}$ is a vector of length $n$ that contains the design variables, $c(\boldsymbol{x})$ contains the nonlinear constraint functions, and $A$ is the linear constraint matrix. Note that $\boldsymbol{u}$ and $\boldsymbol{l}$, the upper and lower bounds, are vectors and thus are specified for each variable and constraint.

The optimizer uses a sequential quadratic programming algorithm to look for the minimum of $F(\boldsymbol{x})$. Within each iteration, the search direction is the solution of a quadratic programming (QP) problem. Each QP subproblem is solved by a quasi-Newton algorithm. The optimizer stops when it finds a local minimum of $F(\boldsymbol{x})$.

The user needs to define $F(\boldsymbol{x})$, $A$, $c(\boldsymbol{x})$, and the bounds for each, as well as an initial estimate of the solution. An important consideration is the difference intervals used in the finite difference approximation of the gradient. NPSOL has an option to calculate the difference interval; however, this involves a large number of calls to the flow solver, which is impractical. A common difference interval for all design variables is specified as an input throughout this study.

## Results and Discussion

In this section, a wind-tunnel test case of an H-A body is considered. The CFD code and the optimizer are coupled to modify the body shape of the H-A body to minimize the drag. Both viscous and inviscid CFD calculations were performed to compare the results. A grid refinement study is also presented in this section.

### Test Cases

In the experimental study,[9] the H-A body had a length $L$ of 36 in. with a fineness ratio $L/2r_{max}$ of 7. The location of maximum thickness was $x_{max} = 21$ in., $\theta_{max} = \cos^{-1}(\frac{1}{6})$, and $A_{base}/A_{max} = 0.532$.

*Flow Solver*

As a validation test case, the UPS3D code ran in inviscid mode over a range of supersonic Mach numbers. A conic approximation at 1% body length from the nose was made for the initial marching plane of the code. For H-A body, study showed that the approximation at this initial plane gave acceptable error in drag, and the initial plane is far enough to allow the use of a relatively large marching step size (0.1% body lengths). Figure 2 shows that the CFD result compares well with characteristic theory and experimental data. Note the variation of wave drag with Mach number predicted by both the characteristic theory and inviscid CFD solutions. Slender-body theory predicts no variation of drag with Mach number.

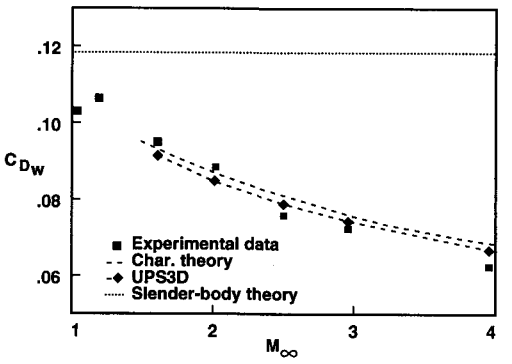


Fig. 2 Wave drag comparison over a range of Mach number, $L/2r_{max} = 7$.

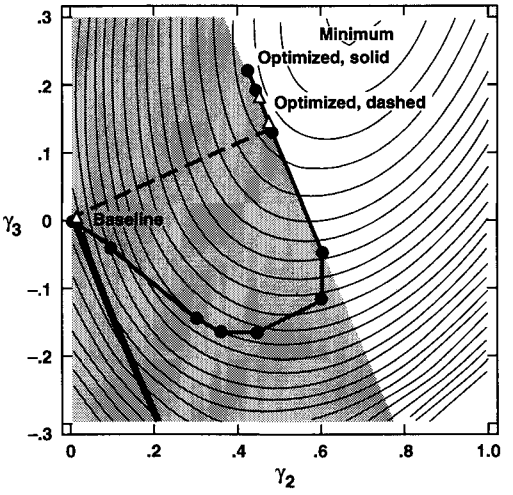


Fig. 3 Constrained optimization paths for difference interval of $\varepsilon = 0.01$ (solid line) and $\varepsilon = 0.005$ (dashed line).

*Optimizer*

As a test case for the optimizer, NPSOL was run using the analytic slender-body formula for drag [Eq. (2)] as the objective function. For this test case, the $\alpha_n$, ($n = 1, 2, \ldots, 5$) coefficients were the design variables, and the constraints C1 through C3 were implemented. The design variables were set to arbitrary nonzero values. Within six iterations the optimizer minimized $C_{Dw}$ by locating $\alpha_1$ and $\alpha_2$ at the slender-body predicted values, and setting $\alpha_3$ through $\alpha_5$ to zero.

In order to visualize the process of optimization, a two-design-variable ($\gamma_2$ and $\gamma_3$) case is considered. Figure 3 is a contour plot of the wave drag coefficient with respect to $\gamma_2$ and $\gamma_3$. The dots and triangles in the figure are iterative points in the optimization. Linked together, they form a search path. The thickest solid line satisfies the equation $dA/dx|_{x=21} = 0$, and the shaded area satisfies the inequality $-1 \leq dA/dx|_{x=21} \leq 1$, [Eq. (7)], which is the constraint used. Note that for a fineness ratio of 7, H-A has maximum radius at $x = 21$. The thinner solid line and the dashed line are search paths used by NPSOL with difference intervals of $\varepsilon = 0.01$ and $\varepsilon = 0.005$, respectively. The larger difference interval calculates a less accurate gradient, and thus locates a minimum more slowly than the smaller difference interval. However, there are two local minima in this design space along the constraint boundary. The larger difference interval found the better of the two minima. The smaller difference interval stopped be-

fore it found that minimum. This is not always the case, as a larger difference interval could miss a local minimum by "stepping" over it entirely.

### Inviscid Optimization

The inviscid optimization process gave the result shown in Fig. 4 for a freestream Mach number of 2.5 and an angle of attack of 0 deg. The sectional wave drag coefficient is plotted along with the radius of the original and optimized shapes. During optimization the volume of the forebody is reduced in order to improve the sectional wave drag in this region. The improvement over the original H-A body is reduced aft of the maximum cross-sectional area because of an increase in volume that occurred satisfying the constraints C1 and C2. Overall, the wave drag of the H-A body was reduced by 5%. Although the optimized body was designed at Mach 2.5, Fig. 5 shows that the same optimized body gives lower drag than the H-A body at other Mach numbers. Using $\varepsilon = 0.01$, 48 new body shapes were generated and analyzed to reach this result. The whole process took approximately 2.5 CPU hours on the Cray Y-MP. Each flow solution calculated by UPS3D uses 160 s, with an additional 1.3 s in grid generation.

### Viscous Optimization

The same design procedure was also performed with viscosity in laminar flow taken into account. The result is shown in Fig. 6. The optimizer took much the same strategy as the inviscid case in that the nose of the body was reduced, while a penalty was paid at the rear of the body. The viscous drag results include both wave and skin friction drag, so while the actual drag reduction is comparable to the inviscid optimization, the improvement in this case is 4%. Figure 7 shows that the same body gives lower drag than the original at other Mach numbers. This optimization process with $\varepsilon = 0.01$ took about 3.5 CPU hours total on the Cray Y-MP and employed 40 flow solutions. Each solution took UPS3D 320 s, with an additional 1.3 s utilized in grid generation. Table 1 gives the values of the design variables for the inviscid and viscous optimization processes.

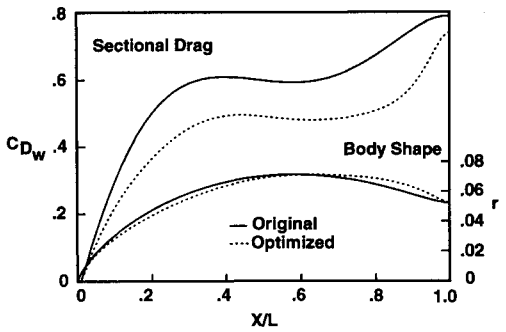


Fig. 4 Inviscid optimization with five design variables; $M_\infty = 2.5$, $L/2r_{max} = 7$.

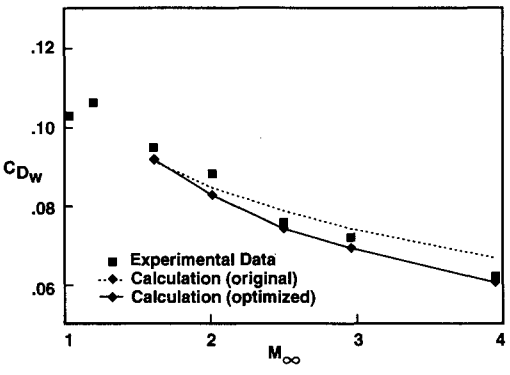


Fig. 5 Wave drag comparison between the original H-A body and the H-A body optimized at $M_\infty = 2.5$, over a range of Mach numbers, $L/2r_{max} = 7$.

### Off-Design Performance

The effects of off-design angle of attack $\alpha$ and Reynolds number on the performance of the new, optimized shape were also investigated. For the body that was optimized at 0-deg angle of attack, the effects of nonzero angles of attack are shown in Fig. 8. As $\alpha$ increases, the reduction of drag vs the original decreases slightly.

The lower half of Fig. 9 indicates the radial distribution results of three optimization processes at differing Reynolds

Table 1 Optimized design variables

| | $\gamma_1$ | $\gamma_2$ | $\gamma_3$ | $\gamma_4$ | $\gamma_5$ |
|---|---|---|---|---|---|
| Inviscid | 0.853 | 0.673 | 0.495 | 0.420 | 0.0846 |
| Viscous | 0.679 | 0.598 | 0.353 | 0.264 | 0.01875 |

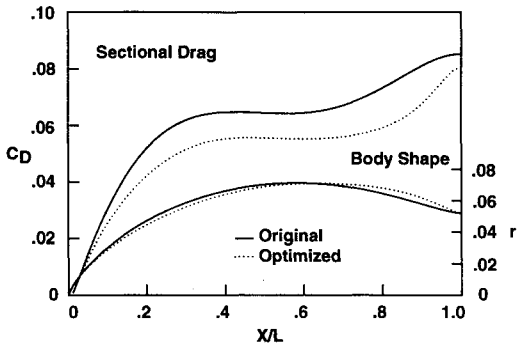


Fig. 6 Parabolized Navier-Stokes optimization with five design variables, $M_\infty = 2.5$, $L/2r_{max} = 7$, $Re = 9 \times 10^6$.

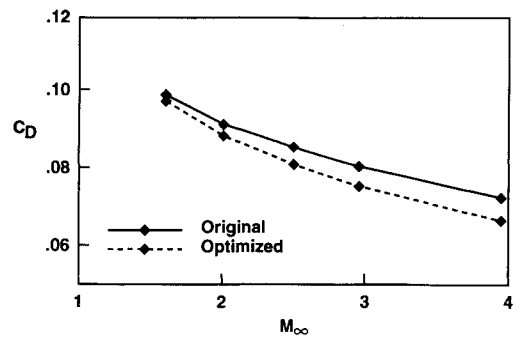


Fig. 7 Total drag comparison between the original H-A body and the H-A body optimized with five design variables at $M_\infty = 2.5$, over a range of Mach numbers, $L/2r_{max} = 7$, $Re = 9 \times 10^6$.

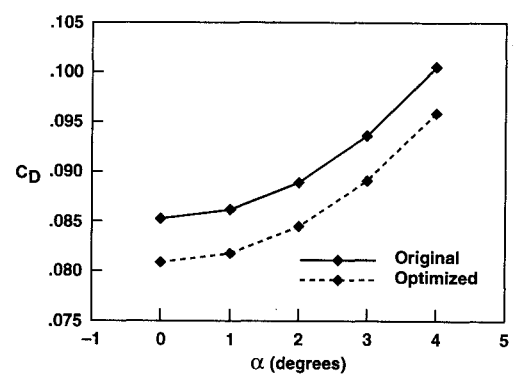


Fig. 8 Total drag comparison between the original H-A body and the H-A body optimized with five design variables at $M_\infty = 2.5$ and $\alpha = 0$, over a range of Mach numbers, $L/2r_{max} = 7$, $Re = 9 \times 10^6$.

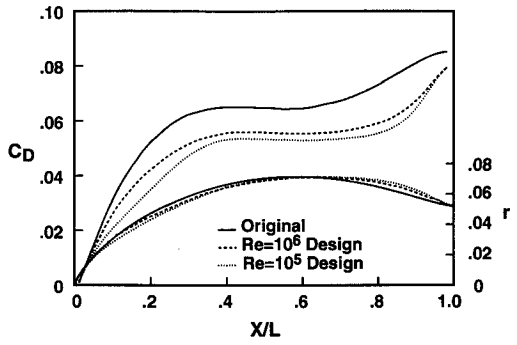


**Fig. 9 Total drag comparison between the original H-A body and the H-A body optimized with five design variables at $M_\infty = 2.5$ and $\alpha = 0$, for $Re = 10^6$, and $Re = 10^5$ computed at $Re = 10^6$, $L/2r_{max} = 7$.**

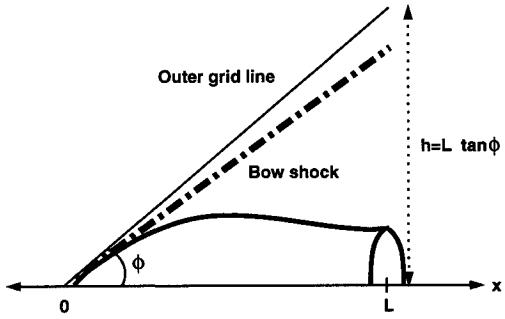


**Fig. 10 Relationship between the size of the computational grid and the bow shock.**

numbers. The solid line is the original H-A body, the dashed line is the body optimized at a Reynolds number of $10^6$, and the dotted line is the body optimized at a Reynolds number of $10^5$. The sectional total drag coefficient of these three configurations calculated at a Reynolds number of $10^6$ is shown in the upper half of the figure. The lower Reynolds number case, which features thicker boundary layers, and hence greater flow displacement, shows the largest perturbation in geometry from the H-A body.

### Grid Refinement

A calculation performed on a coarse grid will, in general, contain a larger numerical error than one performed on a fine grid. However, the coarser grid will, in most cases, run significantly faster. It is desirable to reduce the computer time by using the coarsest grid possible that will still yield a physically accurate result. The key to running an optimizer/flow solver efficiently is to choose a sufficiently coarse grid so that the cumulative CPU time does not become excessive, yet a fine enough grid to locate a physically valid optimum.

In this grid-refinement study, an optimization problem at Mach 2.5 and 0-deg angle of attack was considered. The computational grid had 21 points in the circumferential direction and the step size of the UPS3D code was taken to be 0.1% of the body length. The grid resolution in the circumferential direction and the step size were fine enough to be kept fixed; only the number of grid points $P$ in the normal direction was altered. The distance between the first grid point (in the normal direction) and the surface grid is less than or equal to $s = 0.5(h/P)$, where $h$, given by $L \tan \phi$, is the vertical distance from the end of the body to the outer grid (see Fig. 10). Due to grid effects, the calculated bow shock position of the H-A body differed with grid density until the grid was dense enough to resolve the physical shock location. For each computational grid, the angle $\phi$ was chosen so that the bow shock was as close as possible to the outer boundary. Table 2 gives the values of $\phi$ and $s$ with different computational grids.

**Table 2 Normal grid points vs shock location**

| Grid points, $P$ | $\phi$, deg | Spacing, $s/L$ |
|---|---|---|
| 10 | 50 | 0.060 |
| 20 | 42 | 0.025 |
| 30 | 38 | 0.013 |
| 40 | 36 | 0.009 |
| 50 | 32 | 0.006 |
| 60 | 31 | 0.005 |
| 70 | 30 | 0.004 |
| 95 | 30 | 0.003 |

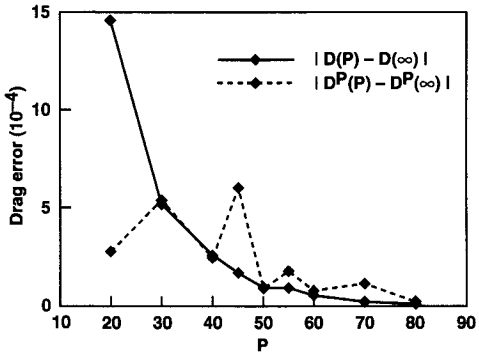


**Fig. 11 Comparison of the error due to grid density (normal direction) of the original body vs the modified body. The modified body has been optimized at each of the normal point grids.**

The behavior of the flow solution and optimization results on the various grids are analyzed to characterize the errors arising from grid density. For clarification, the following definitions are introduced:

$D(P) \equiv C_D$ calculated on a $P$-point H-A grid
$D(\infty) \equiv C_D$ calculated on an asymptotic H-A grid (approximated by 95 points)
$D^m(P) \equiv C_D$ calculated on a $P$-point grid whose surface shape is obtained in an optimization process on an $m$-point grid
$\Delta D^P(P) \equiv |D^P(P) - D^\infty(\infty)|$ the approximate drag reduction of a new design which was obtained by the optimization process on a $P$-point grid
$\Delta D^P(\infty) \equiv |D^P(\infty) - D^\infty(\infty)|$ the actual drag reduction of the new design which was obtained by the optimization process on a $P$-point grid

The errors due to grid density in the CFD computations of the H-A body and the optimized design are given by $|D(P) - D(\infty)|$ and $|D^P(P) - D^P(\infty)|$, respectively. Both curves are plotted in Fig. 11 and show a roughly exponential decay in error due to grid density. This exponential decay in error is common in grid refinement. Figure 12 reveals the grid effect in the optimization process and the CFD calculations. The dashed curve is the error due to grid density in the optimization process, given by $\Delta D^P(P)$. The solid curve is the error due to grid density in optimization and the CFD calculation, given by $\Delta D^P(\infty)$.

Figure 12 indicates that if $3.0 \times 10^{-4}$ error is accepted, the number of grid points needed is as little as about 30 to 40. Review the structure of the CFD grid in Fig. 1 that 40 points may be course near the end of the body; however, it is not that course near the nose. For this type of body, wave drag is mainly contributed by region near the nose because of the radius variation. Thus, as long as the CFD calculations capture the physics contributed to the objective function, the optimization process can locate a physical optimum without having an overly fine grid.

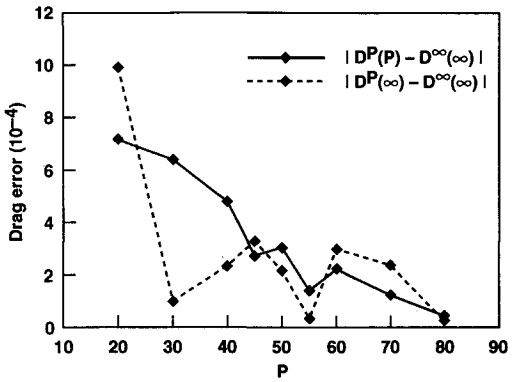


**Fig. 12 Effects of the number of grid points in the normal direction on the optimization process.**

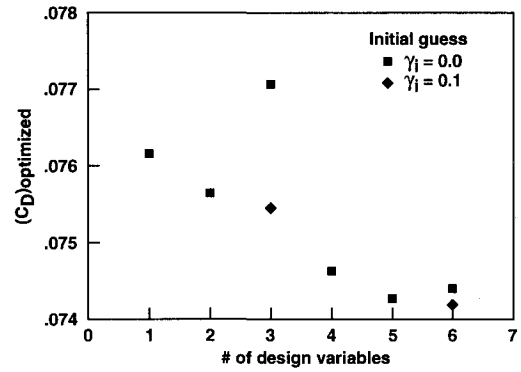


**Fig. 13 Effects of number of design variables and their initial values on the optimized wave drag; $M_\infty = 2.5$, $L/2r_{max} = 7$.**

### Design Variables

As the number of design variables increases, so do the DOF of the optimization process. Often, the larger the number of design variables in the optimization process, the larger the reduction in drag. Figure 13 displays the optimized $C_{Dw}$, from inviscid flow solutions with Mach 2.5 under different numbers of design variables. Each square in the figure represents the drag coefficient obtained from the optimization process with an initial guess of $\gamma_i = 0$, $i = 1 \ldots N$. Thus, as a baseline, the original H-A body is employed. Each diamond represents an initial guess of $\gamma_i = 0.1$, $i = 1 \ldots N$. For the cases with three and six design variables, the optimized $C_{Dw}$ does not quite follow the expected reduction in $C_{Dw}$. This is due to a local minimum around the baseline H-A body for those sets of design variables. By adjusting the initial guess the expected result is obtained.

## Conclusions

A fully automated aerodynamic optimization procedure has been developed that uses CFD to evaluate aerodynamic performance metrics, and numerical optimization to develop improved designs. The present implementation uses a parabolized Navier-Stokes solver for aerodynamic analysis of viscous or inviscid supersonic flows over a minimum-drag body of revolution. Using a CFD solver to calculate the flow produces a slightly different design that has up to 5% lower drag than the original minimum-drag body derived from slender body theory. Although the test configuration was simple, the results demonstrated that the use of Fourier coefficients (having compact definition of the design space), as design variables provided an opportunity for significant drag reduction on more complex configurations as well, such as wing bodies. Using CFD for aerodynamic optimization is a computationally expensive option. A grid refinement study showed that this expense can be partially offset by using coarse grids, as long as the errors associated with grid resolution do not invalidate the physics contributing to the objective function.

## References

[1]Dulikravich, G., "Aerodynamic Shape Design and Optimization: Status and Trends," *Journal of Aircraft*, Vol. 29, No. 6, 1992, pp. 1020–1026.

[2]Malone, J., Vadyak, J., and Sankar, L., "Inverse Aerodynamic Design Method for Aircraft Components," *Journal of Aircraft*, Vol. 24, No. 2, 1987, pp. 8, 9.

[3]Bell, R., and Cedar, R., "An Inverse Method for the Aerodynamic Design of Three-Dimensional Aircraft Engine Nacelles," *Proceedings of the 3rd International Conference on Inverse Design Concepts and Optimization in Engineering Science (ICIDES-III)*, edited by G. S. Dulikravich, ICIDES, Washington, DC, 1991, pp. 405–418.

[4]Haney, H. P., Johnson, R. R., and Hicks, R. M., "Computational Optimization and Wind Tunnel Test of Transonic Wing Designs," AIAA Paper 79-0080, Jan. 1979.

[5]Cosentino, G. B., and Holst, T. L., "Numerical Optimization Design of Advanced Transonic Wing Configurations," NASA TM 85950, May 1984.

[6]Vanderplaats, G. N., and Hicks, R. M., "Numerical Airfoil Optimization Using a Reduced Number of Design Coordinates," NASA TM X-73, 151, July 1976.

[7]Ta'asan, S., "One Shot Methods for Optimal Control of Distributed Parameters System I: Finite Dimensional Control," Inst. for Computer Applications in Science and Engineering, ICASE Rept. 91-2, Jan. 1991.

[8]Ta'asan, S., Kuruvila, G., and Salas, M., "Aerodynamic Design and Optimization in One Shot," AIAA Paper 92-0025, Jan. 1992.

[9]Reuther, J., and Jameson, A., "Control Theory Based Airfoil Design for Potential Flow and a Finite Volume Discretization," AIAA Paper 94-0499, Jan. 1994.

[10]Adams, A. C., "Determination of Shapes of Boattail Bodies of Revolution for Minimum Wave Drag," NACA TN-2550, 1951.

[11]Haack, W., "Projectile Shapes for Smallest Wave Drag," Air Force Material Command, U.S. Air Force, Brown Univ., Translation A9-T-3, Contract W33-038-ac-15004 (16351), ATI 27736, Providence, RI, 1948.

[12]Sears, W. R., "On Projectiles with Minimum Wave Drag," *Quarterly Applied Mathematics*, Vol. IV, No. 4, 1974, pp. 361–366.

[13]Harris, R., and Landrum, E., "Drag Characteristic of a Series of Low-Drag Bodies of Revolution at Mach Numbers from 0.6 to 4.0," NASA TN D-3163, Dec. 1965.

[14]Ashley, H., and Landahl, M., *Aerodynamics of Wings and Bodies*, Addison-Wesley, Reading, PA, 1965, pp. 99–123.

[15]Sears, W., "General Theory of High Speed Aerodynamics—Part C: Small Perturbation Theory," *High Speed Aerodynamics and Jet Propulsion*, Vol. VI, Princeton Univ. Press, Princeton, NJ, 1954, pp. 61–121.

[16]Lawrence, S., Chaussee, D., and Tannehill, J., "Application of an Upwind Algorithm to the 3-D Parabolized Navier-Stokes Equations," AIAA Paper 87-1112, June 1987.

[17]Chan, W., and Steger, J., "A Generalized Scheme for Three-Dimensional Hyperbolic Grid Generation," AIAA Paper 91-1588, June 1991.

[18]Gill, P., Murray, W., Saunders, M., and Wright, M., "User's Guide for NPSOL: A Fortran Package for Nonlinear Programming," Dept. of Operations Research, Stanford Univ., TR SOL 86-2, Stanford, CA, 1986.